



Article

Distinguishing Features of Quenched Nanoprecipitates in Allotriomorphic Ferrite and Reverted γ during Aging for Dual-Phase PHSS

Ping-Jui Yu ¹, Tzu-Ching Tsao ² , Cheng-An Hsu ¹, Neng-Hao Gan ¹, Shing-Hoa Wang ^{1,*}, Jer-Ren Yang ² , Horng-Yi Chang ³ and Tsai-Fu Chung ⁴

¹ Department of Mechanical Engineering, National Taiwan Ocean University, Keelung 202301, Taiwan
² Department of Materials Science and Engineering, National Taiwan University, Taipei 106216, Taiwan
³ Department of Marine Engineering, National Taiwan Ocean University, Keelung 202301, Taiwan
⁴ Department of Materials Science and Engineering, National Yang Ming Chiao Tung University, Hsinchu 300093, Taiwan
* Correspondence: shwang@email.ntou.edu.tw

Abstract: A novel dual-phase PHSS consisting of lath martensite plus allotriomorphic δ ferrite (ALF) with nanoprecipitates was characterized by high-resolution field emission transmission electron microscopy for quenched, solid-solution-treated, and aged stainless steel. The effects of aging at various durations prior to H₂O or liquid N₂ quenching were investigated. Cu-rich nanoprecipitates evolve from body-centered cubic clusters to 9R Cu under quenching to 3R Cu and subsequently to face-centered cubic ϵ -Cu at various aging durations. Maximum hardness was observed after aging at 600 °C for 1 h. However, after this aging, both reversed austenite and Cu-rich nanoprecipitates coexisted in the martensite matrix. The segregation and diffusion of austenite-stabilizing elements promoted the nucleation of reversed austenite.



Citation: Yu, P.-J.; Tsao, T.-C.; Hsu, C.-A.; Gan, N.-H.; Wang, S.-H.; Yang, J.-R.; Chang, H.-Y.; Chung, T.-F. Distinguishing Features of Quenched Nanoprecipitates in Allotriomorphic Ferrite and Reverted γ during Aging for Dual-Phase PHSS. *Metals* **2023**, *13*, 625. <https://doi.org/10.3390/met13030625>

Academic Editor: José Valdemar Fernandes

Received: 12 February 2023

Revised: 17 March 2023

Accepted: 18 March 2023

Published: 21 March 2023



Copyright: © 2023 by the authors. Licensee MDPI, Basel, Switzerland. This article is an open access article distributed under the terms and conditions of the Creative Commons Attribution (CC BY) license (<https://creativecommons.org/licenses/by/4.0/>).

Keywords: dual phases; allotriomorphic δ ferrite (ALF); Cu-rich nanoprecipitates; precipitation-hardened stainless steel

1. Introduction

Precipitation-hardened (PH) alloy 17-4 PH (AISI type 630 or UNS S17400) is a martensitic stainless steel (SS) containing approximately 3~5 wt.% Cu strengthened by the precipitation of highly dispersed Cu-rich particles inside the tempered lath martensitic matrix and a small fraction of delta ferrite [1–5]. Since 17-4 PH stainless steel has the characteristics of anticorrosion, resistance to abrasion, and high strength, it is usually used in environments with high temperature and high pressure [6]. Stainless steels of 17-4 PH have been used for a variety of applications in steam turbines, marine construction, the chemical industry, and power plants [7] due to its proper combination of mechanical properties and corrosion resistance [8]. After solution treatment, 17-4 PH exhibits a martensitic microstructure but insufficient hardness. Subsequent precipitation aging treatment at temperatures between 480 °C and 620 °C results in a submicroscopic, copper-rich phase and increases hardness and strength [8].

In general, the maximum strength and hardness values can be obtained after initial aging at 450 °C~510 °C, during which the precipitation of coherent copper-rich clusters occurs [8]. Aging at a temperature above 540 °C results in the precipitation of incoherent fcc copper-rich precipitates, lower strength and hardness, and enhanced toughness [8]. At higher aging temperatures, around 580 °C and above, a lamellar-like matrix structure and the formation of a reversed austenite phase are observed [9].

The formation of delta ferrite during the high-temperature process can be examined in the carbon phase diagram and thermal Calc predictions of the 17-4 PH stainless steel [10–12]. The phase diagram shows that the formation reaction of delta ferrite is strongly affected

by the carbon content. Lower amounts of carbon increase the quantity of delta ferrite [12]. The δ phase, originating from homogenization treatment at 1290 °C, was located within the region in which phases $\delta + \gamma$ coexisted [10,11].

Allotriomorphic ferrite (ALF) and idiomorphic ferrite (IDF) have been categorized as the products of diffusional decomposition from austenite, and their distinct morphological difference is believed to be highly related to their nucleation sites. For ALF, the nucleus first forms on the prior austenite grain (PAG) boundary, and then growth follows, either along or normal to this boundary, with the former obviously occurring at a much higher rate. On the other hand, IDF has been reported to form within PAG, and the nucleation of this intragranular ferrite has been assumed to be closely related to inclusions or carbides [13]. The main factors affecting δ ferrite formation were inclusion characteristics, cooling rate, PAG size, etc. After the target temperature was above 1200 °C, the average grain size of prior austenite increased rapidly [14]. With the increase in target heating temperature, the PAG size increased, and the grain boundary area per unit volume decreased, which resulted in the nucleation sites of boundary ferrite (i.e., ALF) being reduced, while the volume fraction of intragranular ferrite (i.e., IDF) began to rise [14–16].

Reversed austenite, which forms during aging at temperatures above 550 °C [17,18], also plays a crucial role. The mechanism of its formation is still not clearly understood, but it has been postulated that the localized segregation of austenite-stabilizing elements such as Cu, Ni, and carbon reduces the austenitizing temperature [2,4]. It also leads to a decrease in the M_s temperature in a localized region in the material, resulting in the stabilization of reversed austenite at room temperature [2,4]. The slower rate of heating results in the precipitation of copper-rich phases and carbides and in the segregation of these atoms towards lath boundaries. Consequently, the bulk of the martensite laths become depleted in copper, an austenite stabilizer, and as a result, the austenite start temperature (A_s) is raised. The lath boundaries, in contrast, become enriched with copper; consequently, the temperature in these regions is depressed, facilitating austenite formation. Since this steel is used in high-temperature applications, evaluating their microstructures and mechanical properties at different age hardening times with 600 °C is important.

2. Materials and Methods

The precipitation-hardened stainless steel UNS S17400 (AISI 630), commonly known as 17-4 PH, in the form of as-received solid-solution-treated 17-4 PH round bars with a diameter of 17 mm, was used as an experimental material. The chemical composition of 17-4 PH, analyzed by glow discharge spectrometer (GDS), is listed in Table 1. All the steel bars were sealed in vacuum quartz tubes and homogenized at 1290 °C, the dual-phase ($\delta + \gamma$) region [10], for 72 h (Figure 1), and then quenched in water. For the bulk material, prior-homogenized specimens were solid-solution-treated at 1145 °C of the dual-phase region and held for 2 h (Figure 1) before being quenched in H₂O and liquid N₂, respectively. Subsequently, the specimens underwent isothermal aging at 600 °C for 1, 3, and 5 h, respectively, as illustrated in Figure 1. Coupons of 3 mm (W) × 5 mm (L) × 4 mm (H) were cut from the half-radius of the round bar for analysis by optical microscopy (OM) and high-resolution transmission electron microscopy (TEM). The observed plane was normal to the rolling direction (RD). The samples were prepared for metallography through a series of mechanical polishing with grit papers of various numbers, then further polished to 0.05 μ m thickness with alumina powder. Samples were immersed for 3–5 min in the reagent Beraha's sulfamic acid etchant, 100 mL H₂O, 3 g K₂S₂O₅, 1 g NH₂SO₃H, 0.5–1 g NH₄FHF [19]. The optical images and area fraction of ferrite were measured based on color metallographic photos and Image J software (1.54b).

Table 1. Chemical composition of 17-4 PH SS (wt.%) by GDS.

Element	C	Si	Mn	P	S	Ni	Cr	Mo	Cu	Al	N	Nb	Fe
Wt.%	0.03	0.37	0.65	0.03	0.03	4.77	15.4	0.13	3.52	0.01	0.018	0.22	bal.

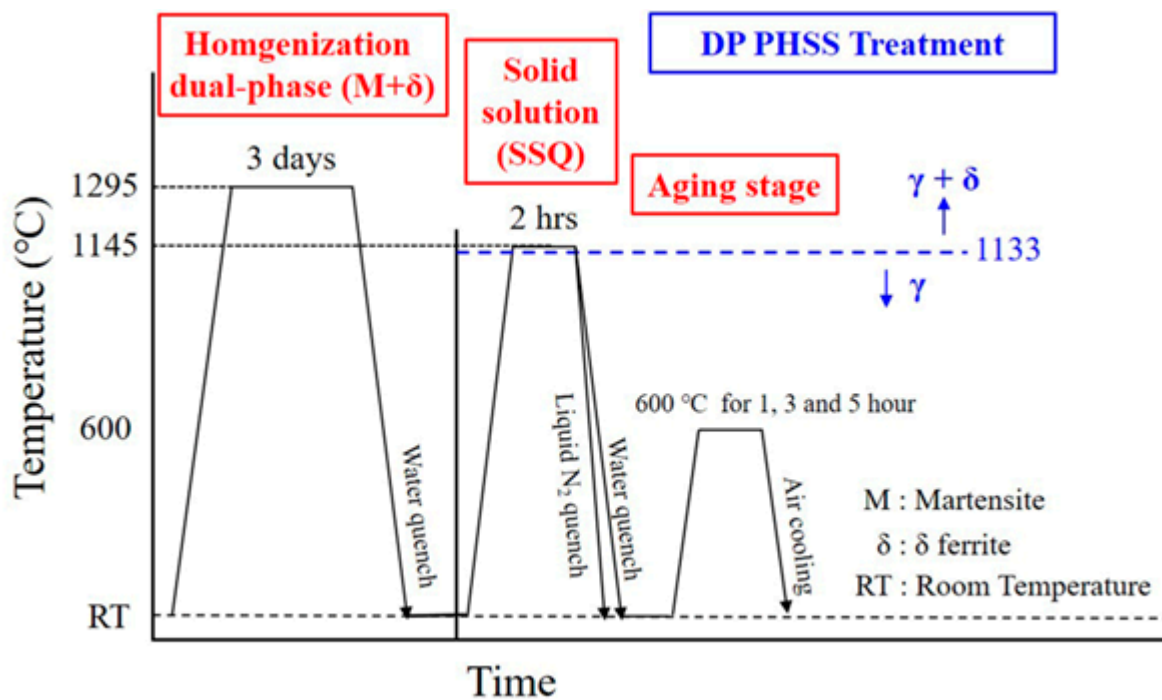


Figure 1. Schematic diagram showing the dual-phase heat treatments and aging at different times.

The microhardness was tested with a load of 300 g for 15 s using an HMV-G20 Vickers microhardness tester. A total of 20 locations with 0.5 mm between indentations were measured, and the average value was regarded as the final hardness. For TEM observation, thin sections were cut from the samples and mechanically polished down to a thickness of 0.2 mm with #800 grit paper and then to 0.1 mm with #1000 grit SiC paper. A 3 mm disk was punched out of the sample and ground to a thickness of 0.05 mm with #1200 grit paper. The disks were electropolished into foils in an electrolyte consisting of 5% perchloric acid, 25% glycerol, and 70% ethanol at -5°C under 35 V potential [20]. The foils were examined under a field emission transmission electron microscope (FE-TEM Tecnai G2 F30) operated at 300 kV.

3. Results

3.1. Dual-Phase Microstructure of Color Metallograph

The optical color microstructures of samples treated after homogenization and solid solution and then quenched in H_2O or liquid N_2 , respectively, are exhibited in Figure 2. Many well-defined large grains of martensite were surrounded by allotriomorphic ferrite (ALF) in white at the grain boundaries, as indicated by the yellow arrows in Figure 2a–c, because of the solid solution treatment in the $\delta + \gamma$ dual-phase region. Allotriomorphic ferrite (ALF) and idiomorphic ferrite (IDF) in Figure 2 have been categorized as the products of diffusional decomposition from austenite, and their distinct morphological difference is believed to be highly related to their sites [13]. For ALF, the nucleus first forms at the prior austenite grain boundary, and then growth follows, either along or normal to this boundary, with the former obviously occurring at a much higher rate. The number of nucleation sites for ALF is proportional to the grain boundary area per unit volume, and therefore can be greatly reduced by increasing the prior austenite grain size, resulting in a layer-like morphology because of the lower possibility of hard impingement between adjacent ALF grains.

On the other hand, IDF, though rarely observed in Figure 2, has been reported to form within prior austenite grains, and the nucleation of this intragranular ferrite has been assumed to be closely related to inclusions or carbides. Previous studies have suggested that IDF tends to nucleate at inclusions such as MnS , Ti_2O_3 , or mixtures of MnS and either

V(C, N) [21] or Al_2O_3 . The prior austenite grain size (PAGS) of homogenization was approximately $164 \pm 23 \mu\text{m}$ (Figure 2a) with about 12 vol% ALF δ . The measured PAGS for two cooling conditions after solid solution treatment were approximately $130 \pm 14 \mu\text{m}$ for H_2O quenching (Figure 2b), and $142 \pm 17 \mu\text{m}$ for liquid N_2 quenching (Figure 2c). Color metallography highlighted the δ ferrite grains in various heat-treated 17-4 PH SS, as shown in Figure 2. Even after subsequent solid solution treatment, the prior ALF δ continued to grow to about 22 vol% ALF δ for H_2O quenching, and about 15 vol% ALF δ for liquid N_2 quenching. The faster cooling in liquid N_2 resulted in larger PAGs, leading to a lower vol% ALF δ .

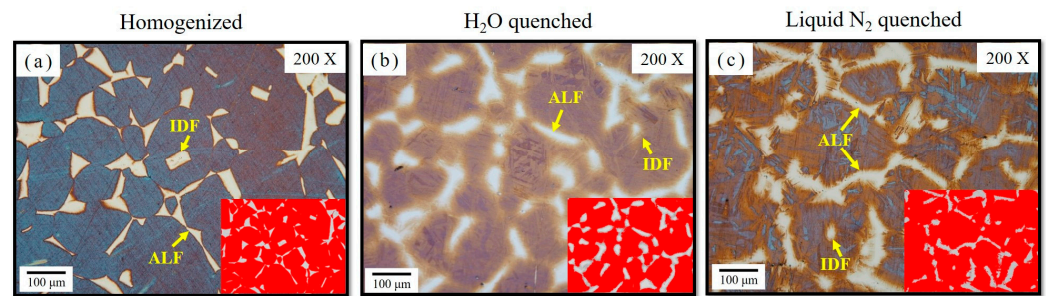


Figure 2. Microstructures of type 17-4 PH color metallography etched with Beraha's sulfamic acid reagent for (a) water quenched homogenization; (b) water quenched solid solution; (c) liquid nitrogen quenched solid solution. (Image J pictures for phase volume measurement inserted at the bottom right).

3.2. Hardness Distributions

Vickers hardness values (HV) obtained for the homogenized samples, solid-solution-treated samples, and samples aged under 600°C conditions are plotted in Figure 3. The average microhardness was about 287 HV in H_2O -quenched homogenization, and rose to about 303 HV due to the formation of microtwins during either H_2O - or liquid N_2 -quenched solid solution treatment, as depicted in Figure 3. For aging at the temperature of 600°C for 1 h, the hardness value exhibited a peak value then decayed from the peak hardness, with the prolonged aging time, to approaching the solid solution hardness of about 303 HV of aging for 5 h at 600°C . An inappropriate aging temperature has the drawback of softening the steel by coarsening the microstructure, as shown in Figure 3.

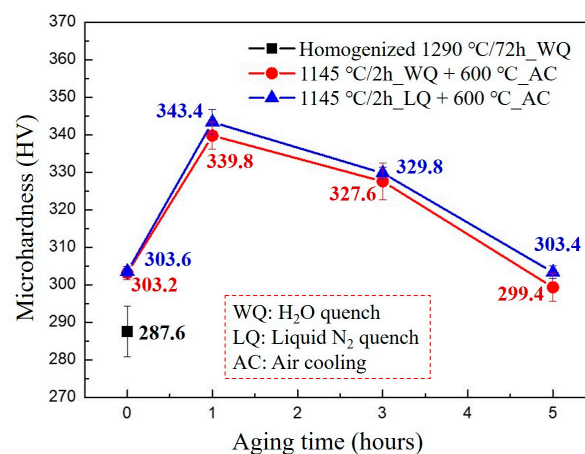


Figure 3. The effects of various aging times with different cooling methods on the hardness distribution of 17-4 PH SS.

3.3. Quenched Nanoprecipitate Formation in ALF δ Matrix

The microstructure of the homogenized steel and H_2O -quenched (WQ) steel is composed basically of a dual phase in lath martensite and δ -ferrite, as shown in Figure 4.

The explanation in regard to the formation of lath martensite in the very low carbon content of 0.03 wt.% of 17-4 PH steel can be rationalized in terms of high M_s (martensite transformation start temperature), which is around 93–170 °C, and the alloying effect in very-low-carbon alloy steel. Typically, plate martensite is produced in high-carbon alloys with more than 1.0% carbon, while lath martensite is the sole product in low-carbon alloys with less than about 0.6% carbon. The width of the martensite laths in the homogenized steel was less than 0.4 μm without the precipitates inside the laths (Figure 4a). Generally, no copper nanoparticles were found in martensite laths besides the high density of dislocations, indicating that the martensite phase was supersaturated with Cu atoms in the homogenized condition [22] in Figure 4a,b. Nevertheless, it does not obey the conventional understanding of aging precipitation that the numerous nanoparticles of Cu-rich precipitates were embedded in ALF δ -ferrite matrix immediately after H_2O quenching, as can be seen in Figure 4c,d. It has been confirmed and published by thermodynamic prediction [10]. Quenching from elevated temperatures to low temperatures can lead to excess vacancies; that is, more vacancies than the equilibrium state at low temperature, which can accelerate the precipitation processes. Based on the Thermal-Calc calculated predictions for the phase and Cu solubility [10], the experimental results indicated that Cu-rich nanoparticles precipitated instantly during quenching from ultrasupersaturated ALF δ ferrite. They also verified the presence of Cu solubility at high solid solution temperature under the coexistence of BCC δ and FCC γ [10]. Normally, Cu-rich precipitates are commonly found in supersaturated solid solution during subsequent aging treatment because of the decrease in the solubility of copper in ferrite with decreasing temperature [23].

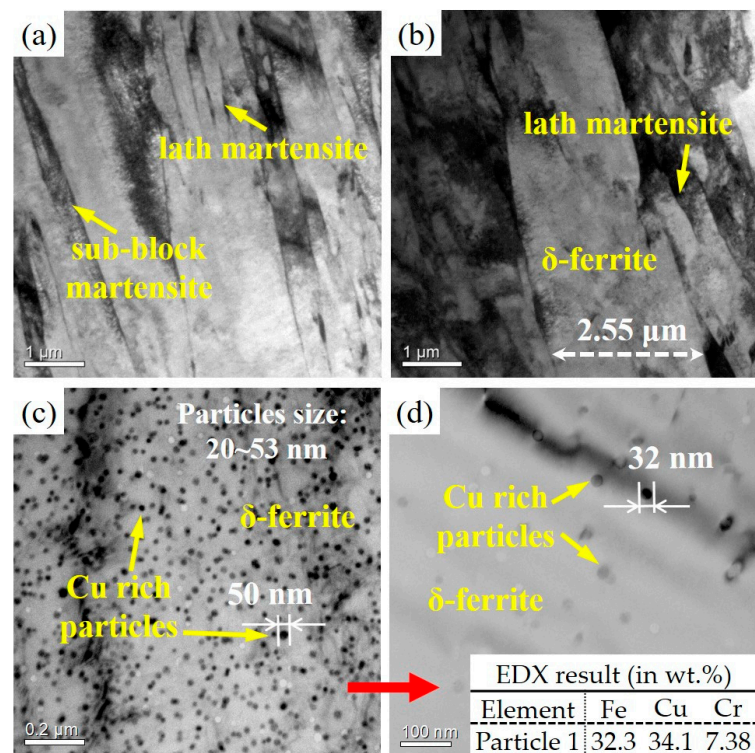


Figure 4. Bright-field image of (a) lath martensite and sub-block martensite, (b) δ -ferrite in 17-4 PH SS after homogenization. (c) Many fine Cu-rich nanoparticles existed in the δ -ferrite matrix. (d) EDX spectra of Cu-rich particles.

The formation of nanoprecipitates during quenching is rarely observed, and distinguishes this process from conventional aging precipitation. An analysis of nanomechanical properties revealed that the strength of ALF δ ferrite containing Cu-rich nanoparticles is superior to that of martensite [10,11].

Similarly, many Cu-rich nanoparticles also existed in the δ ferrite matrix after either the H_2O -quenched or the liquid N_2 -quenched solid solution treatment, as depicted in Figure 5. In addition, the striking feature of microtwins was also found inside the martensite laths. The existence of twin-related streaks was interpreted as a result of the accommodation of the strain created by the adjacent laths. The diffraction patterns were obtained along $[113]_{bcc}$ in Figure 6a and $[011]_{bcc}$ in the Figure 6b axis zones, which were captured from H_2O -quenched (Figure 6a) and liquid N_2 -quenched (Figure 6b) solid solution steel, respectively.

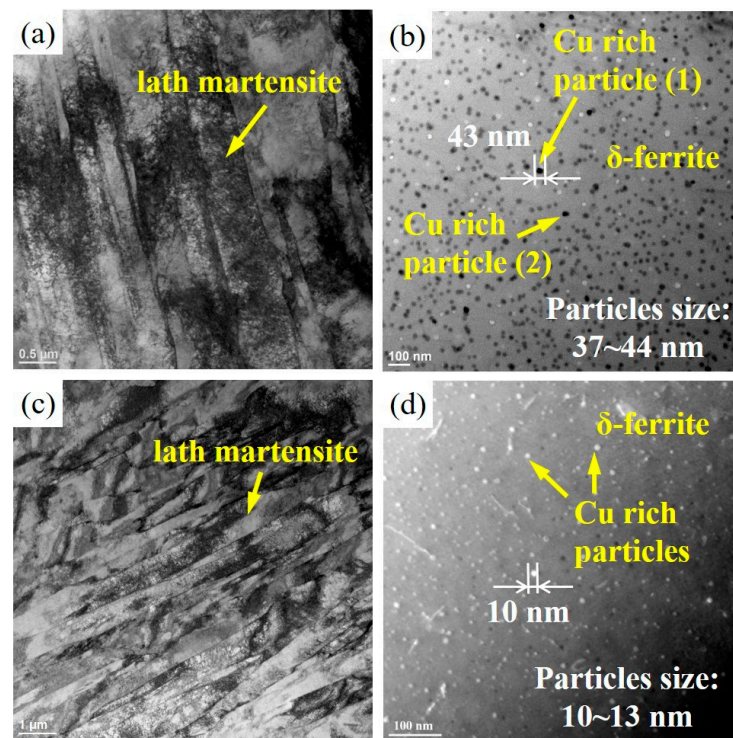


Figure 5. Microstructures of H_2O -quenched solid solution samples for (a) lath martensite and (b) Cu-rich nanoparticles in ferrite; and that of liquid N_2 -quenched samples for (c) lath martensite and (d) Cu-rich nanoparticles in ferrite.

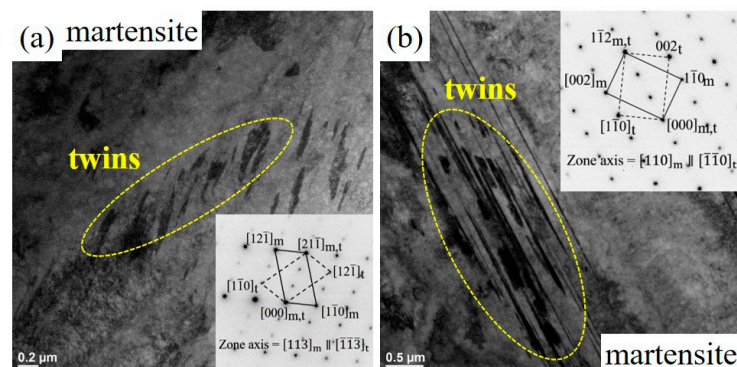


Figure 6. Microtwin images of (a) water- and (b) liquid N_2 -quenched solid solution specimens, along with their diffraction patterns in the bottom-right corner (a) and top-right corner (b).

3.4. Aging Feature of Nanoprecipitates and Reverted γ

The samples with peak hardness at 1 h were selected for TEM examination. The microstructures of aged samples after solid-solution treatment and H_2O quenching (WQ) are presented in Figure 7. By superimposing two periodic structures (i.e., lattices) under the proper conditions, one can obtain a new fringe pattern. This pattern is known as a Moiré

fringe pattern [24,25]. The shape of the copper precipitates tended toward an elliptical shape after aging at 600 °C for 1 h, with a short axis of about 18.3 nm and a long axis of about 24.1 nm, as shown in Figure 7c. The Moiré fringes of parallel bands (Figure 7c) formed on the precipitate; this feature was quite similar to that of the twinned 9R structure reported by Othen et al. [26,27]. It has been confirmed by the two-beam condition to demonstrate the precipitation of bcc Cu-rich precipitates in the bcc ferrite matrix [28]. They suggested that the presence of a strain field without any Moiré fringes in the precipitate area is evidence of the presence of bcc Cu-rich precipitates. It was argued that the formation of $(11\bar{4})_{9R}$ 9R twins in 9R Cu-rich precipitates could reduce the strain energy between 9R Cu-rich precipitates and the α' -matrix during the transformation [29]. The peak hardness after aging at 600 °C for 1 h was higher than the hardness of the solid solution sample shown in Figure 3, which was attributed to the presence of nanocopper precipitates in the lath martensite inhibiting the dislocation motion. Therefore, during aging, copper obtains the thermal energy of diffusion and precipitates from the matrix [3].

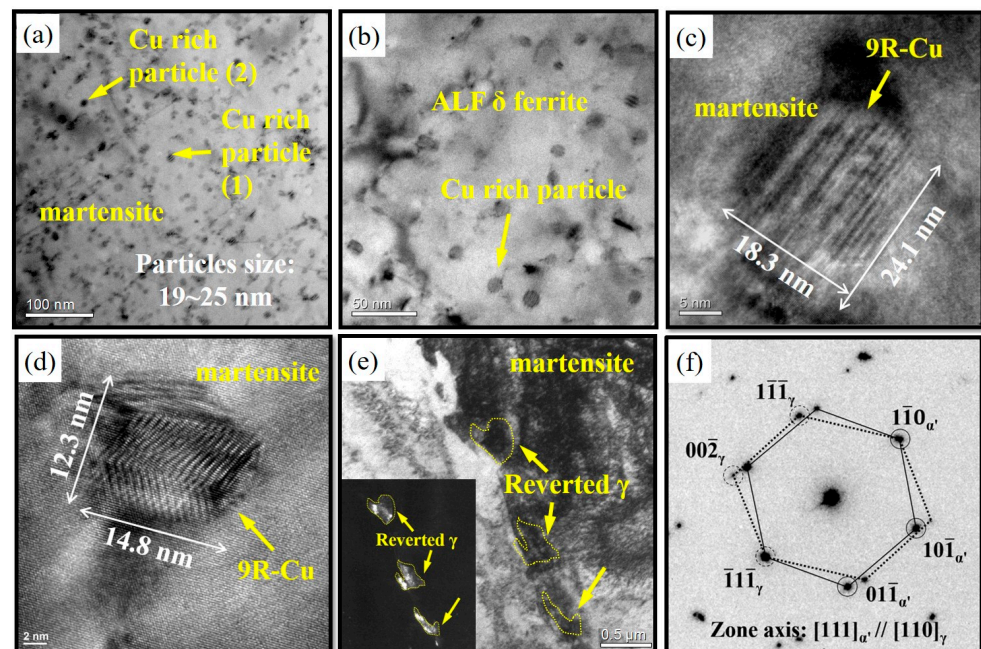


Figure 7. Samples aged for 1 h at 600 °C after H₂O-quenched solid solution treatment. (a) Cu-rich particles in martensite matrix; (b) enlarged magnification of nano Cu-rich particles in ALF δ ferrite matrix; (c) enlarged 9R-Cu in (a) martensite with the Moiré fringes of parallel bands; (d) 9R Cu-rich precipitates with zigzag or herring-bone pattern of interference fringe; (e) collapsed lath martensite embedded reversed γ dark field of reversed γ at bottom left; (f) orientation relationship (OR) between martensite α' and reversed austenite γ .

Reversed austenite was also found in Figure 7e, and its dark field reflection in the bottom left of Figure 7e was taken from the selected area diffraction (SAD) patterns. The SAD patterns produced from the regions of the reversed austenite and martensite matrix are shown in Figure 7f. The orientation relationship between the reversed austenite and the martensite matrix in Figure 7f was analyzed and identified as $(10\bar{1})_{\alpha'} // (1\bar{1}\bar{1})_{\gamma}$; $[111]_{\alpha'} // [110]_{\gamma}$. The morphology of reversed austenite suggests that its formation was involved with a diffusional mechanism [2]. The nano Cu-rich particles still remained within the δ ferrite to this stage.

The microstructures that resulted from aging after previous fast cooling by liquid N₂ (LQ) quenching are presented in Figure 8. The nano Cu-rich particles that precipitated in the martensite matrix were about 6~12 nm; they were smaller than previous water-quenched nano Cu-rich precipitates in size (Figure 8a) due to the faster cooling rate. The

Cu-rich particles formed in a sequence of twinned 9R Cu-rich precipitates with a diameter of 4~17 nm after coherent bcc Cu clusters. They sequentially transformed into the more stable 3R Cu-rich precipitates having the K-S OR with α' .

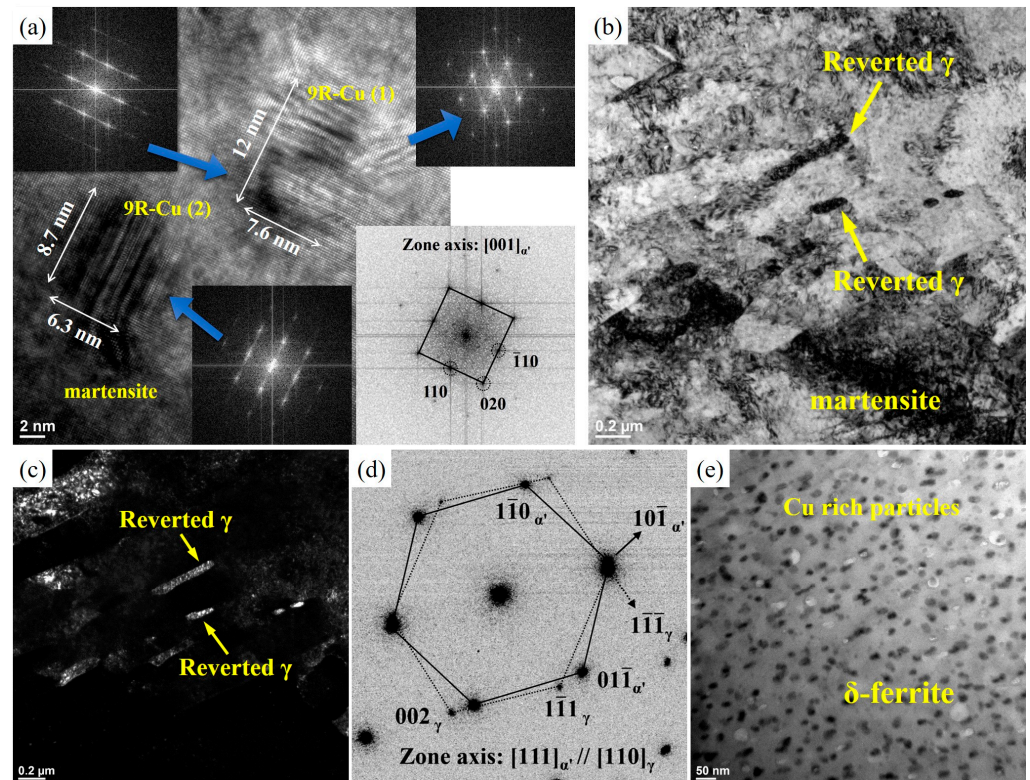


Figure 8. Samples aged after liquid N₂-quenched solid solution treatment. (a) Nano 9R-Cu rich particles in martensite matrix with diffraction patterns; (b) collapsed lath martensite and reversed γ ; (c) dark field of reversed γ ; (d) orientation relationship (OR) between martensite α' and reversed austenite γ ; (e) nano Cu-rich particles in δ ferrite.

In addition, the enlarged image in Figure 8a shows a Moiré fringed particle, defined as a 9R Cu-rich particle, which also precipitated in the martensite matrix, and its diffraction pattern is shown in Figure 8a. These distinct striations perpendicular to the $[001]_{\alpha'}$ direction were observed, and the satellite spots around the $(002)_{\alpha'}$ and $(110)_{\alpha'}$ reciprocal planes appeared in the SAD patterns (Figure 8a). It is worth noting that the bcc Cu clusters were arranged in a regular morphology; that is, they were characterized by a period of distinct striations perpendicular to the $[001]_{\alpha'}$ direction [30]. The pattern also showed streaks along with $[110]_{9R-Cu}$, and other diffraction spots of Cu-rich particles too weak to be recognized. It was concluded that the 9R Cu-rich particles and reversed austenite coexisting in the martensite were predominated by all the Cu atoms that diffused from adjacent supersaturated δ ferrite into the martensite matrix through many short diffusion paths of dislocations, sub-block, and block boundaries, and joined with the supersaturated Cu already in the prior austenite matrix. A similar type of herring-bone image has been documented by several authors [30]. A zigzag or herring-bone pattern of interference fringe was clearly visible within the precipitate, highly suggestive of uniform twin-related bands extending throughout the particle [30]. The observed orientation relationship between the bcc α' and the 9R Cu-rich particles can be expressed as $(001)_{bcc} // (114)_{9R}$; $[1\bar{1}1]_{bcc} // [\bar{1}10]_{9R}$ [20,25]. It has been argued that the formation of $(114)_{9R}$ twins in 9R Cu-rich particles can reduce the strain energy between 9R Cu-rich particles and the α' matrix during the transformation [30].

The bright field and centered dark-field images obtained from the aged steel are shown in Figure 8b,c. The dark field of the reversed austenite pattern in Figure 8d was taken from the SAD in Figure 8b. This analysis confirmed that the reversed austenite preferentially

formed along martensite lath boundaries and inside the martensite laths, which agreed with the literature [31]. The electron diffraction pattern (Figure 8d) indicated that the reversed austenite had an identical K-S OR with the martensite matrix, $(10\bar{1})_{\alpha'}/(1\bar{1}\bar{1})_{\gamma}$; $[111]_{\alpha'}/[110]_{\gamma}$, which was consistent with the literature [32,33]. A certain amount of reversed austenite formed along the original martensite laths, and the mechanism of its formation involved a diffusional mechanism (Figure 8b). The Cu-rich nanoprecipitates still remained within the δ ferrite to this stage in Figure 8e.

4. Discussion

4.1. Unique Characteristics of Quenched Nano Cu-Rich Precipitation in ALF δ Matrix

In the early stage of the precipitation of copper, coherent bcc clusters nucleate and grow in the supersaturated bcc matrix and lose coherency after reaching a certain critical size, and they further grow such that the copper-rich particles became fcc copper-phase precipitates [2,34]. The evolution of Cu-rich precipitates follows the steps of critical size bcc-Cu about 4 nm \rightarrow 9R (coherent) about 4~17 nm \rightarrow 3R (incoherent) about 17~30 nm \rightarrow ϵ -Cu (fcc) [35]. In the literature, it is reported that twinned 9R Cu-rich particles with diameters of 4 nm to 17 nm form after coherent bcc Cu clusters and sequentially transform into more 3R Cu-rich precipitates having a K-S orientation relationship with α' [36]. The precipitates in both binary and ternary alloy specimens were found to have transformed from a roughly spherical twinned 9R structure to an ellipsoidal untwinned 3R structure. The bcc Cu clusters initially form in the α' matrix and show perfect coherency with the α' matrix. After reaching a critical size of ~4 nm, the martensitic transformation of bcc Cu to 9R Cu takes place due to the minimization of large coherent strain energy [27,30,37]. The crystal structure of 9R Cu-rich particles was confirmed to be orthorhombic and contains a high density of twinning caused by misfit strain between bcc and 9R structures. The critical size for the Cu-rich precipitates' transformation is not known precisely, but it must lie in the range of 18~30 nm [27]. The production of such random stacking faults on the close-packed basal planes in the regular 9R structure is believed to occur as a result of the lattice invariant deformation during the martensitic transformation [27].

During aging at 600 °C for 1 h, the highly dispersed, coherent precipitates of copper strongly contribute to the hardening of the alloy. The peak hardness after 600 °C aging (Figure 3) could be explained by the distribution of very fine copper precipitates on dislocations in the martensite and ferrite, which evidently acted as sites for precipitate nucleation and growth [23]. These fine Cu-rich precipitates contributed to strengthening by precipitation hardening, and unresolved bcc clusters and fcc ϵ Cu-rich precipitates provided additional increments in strength. Coarser incoherent copper precipitates have been found to inhibit localized slip and the formation of dislocation pile-ups at grain boundaries. The formation of a very fine Cu-rich precipitate distribution is the principal hardening mechanism in this alloy system.

The formation of coherent Cu-rich precipitates during aging leads to hardening, but microstructure coarsening and modification of the dislocation structure by tempering will decrease the hardness [23]. Thus, an increase in temperature accelerates the aging of the alloy due to the increase in the diffusion rate, which in turn enhances both the nucleation and growth of Cu-rich precipitates. Therefore, the hardness change depends on the temperature and tempering duration. Significant reductions in hardness after aging at 3 h and 5 h were caused by overaging of the martensite and/or the formation of reversed austenite (Figures 7b and 8b). Overaging at 600 °C for a prolonged time at a specific temperature caused the copper atoms to diffuse to the grain boundaries and the boundaries of the martensite laths such that reversed austenite formed at these locations. This brought about the depletion of copper and Ni in the martensite matrix [38]. Overaging is due to the coarsening of incoherent ϵ Cu-rich precipitates and the occurrence of reversed austenite.

4.2. The Reversed Austenite Formation during Aging

The reversed austenite usually appears in two different morphologies: granular, as shown in Figure 7b, and lath-like, shown in Figure 8b. Lath-like austenite forms along the lath boundaries of martensite, as seen in Figure 8b, and sometimes within the lath, and this gradually leads to a lamellar duplex structure of alternating austenite and aged martensite films. However, the granular austenite grows mainly from prior austenite grain boundaries, as shown in Figure 7b, or is formed by the growth of lath-like austenite. It has generally been accepted that granular reversed austenite is the product of a diffusion mechanism [39,40].

The reverse transformation from martensite crystals to the austenite orientation implies an effect of morphological memory of the orientation variant of the prior austenite grain. Initially, the reversed austenite formed at the aging temperature of 600 °C and remained upon subsequent cooling to the ambient temperature (Figures 7b and 8b). The reversed γ transformation that occurred at the temperature of 600 °C below the measured $A_s = 785$ °C [41] suggested that the partitioning of Cu and Ni must have enriched these regions to such an extent. A thin layer of reversed austenite along lath boundaries and the intralath Cu-rich phase observed in Figure 8b corresponded to the literature [4].

Regarding the lower hardness after 600 °C aging at 3 h and 5 h in Figure 3 and the influence of reversed austenite, it has been reported [35] that copper precipitates are expected to be favorable nucleation sites for reversed austenite, since copper and austenite have the same fcc structure with similar lattice parameters. During aging at temperatures equal to or above 600 °C, segregation and diffusion of the austenite-stabilizing elements of Cu, Ni, and Fe will have a profound influence on the precipitates and the martensite matrix, leading to the austenite forming element-enriched areas around the copper precipitates, which could trigger the reversed austenite to nucleate. The Cr content from ferrite conversely decreases the amount of reversed austenite. Therefore, C and N, which are also austenite stabilizers, may concentrate in the reversed austenite. Moreover, the growth of reversed austenite attracts considerable amounts of Cu and Ni from the martensite matrix, since the solubility of these elements in austenite is much higher [2,9]. The reversed austenite is a stable phase only after aging around 620 °C and encompasses the ϵ -copper-rich precipitates [38]. It was reported that the influence of austenite reversal is much more pronounced on softening than the influence of the coarsening of precipitates is [42,43]. Sinha et al. [44] excluded the mechanism of dissolution of precipitates for the formation of reversed austenite. They supposed that Ni diffused to dislocations and defects, resulting in the microsegregation of austenite-stabilizing elements in localized areas. Kim and Wayman [43] suggested that the formation of lath-like austenite in high-Ni maraging alloys is shear-dominated but assisted by a diffusion-controlled process. The habit plane of the lath-like austenite is close to $[111]_\gamma$. All characteristics of the orientation relationship, habit plane, and growth direction are quite similar to those of lath martensite and suggest that lath austenite forms due to a shear mechanism [40,43]. However, based on EDX analysis, the lath-like austenite contains higher Ni and Mn contents than the original martensite does. Thus, it is concluded that diffusion is involved [40,43]. It is possible that at a temperature of 600 °C, Ni, C, and other austenite stabilizers gradually diffuse to the reversed austenite and become trapped there. Because the reversed austenite is stabilized by these alloying elements, carbon is preferentially located in it, alloy carbides fail to precipitate in the martensite, and the martensite is unable to decompose at the aging of one hour.

5. Conclusions

The microstructures of solution-treated 17-4 PHSS were mainly composed of a dual phase in lath martensite and ALF δ ferrite with nanoprecipitates. The most distinctive features were the Cu-rich nanoparticles that appeared in the ALF δ ferrite matrix directly after the quenched homogenization, and the Cu-rich nanoparticles that precipitated in the martensite matrix during aging. The maximum peak aging hardness appeared only after ag-

ing for 1 h at 600 °C. Meanwhile, it was noted that the reversed austenite appeared at 600 °C by alloy diffusion. The nano Cu-rich particles that precipitated in the martensite during aging at 600 °C for 1 h could lead to hardening. However, the coarsening, the degraded lath martensite, the reduction in dislocation density and the growth of the reversed austenite with increases in aging time would result in softening due to a decrease in hardness. The following phenomena occur during the aging treatments: (i) rearrangement of dislocations within the martensite laths; (ii) peak hardness, possibly due to the ultrasupersaturated successive Cu-rich precipitation joined to the previous quenched precipitates in δ ferrite and the new nanoprecipitates occurred in martensite; and (iii) formation of either granular or lath-like reversed austenite along the lath boundaries by austenite stabilizing element partition. The softening effect may be associated with the coarsening of the incoherent ϵ -Cu rich precipitates and the formation of slight amounts of reversed austenite.

Author Contributions: Methodology, data curation, investigation, writing—original draft, P.-J.Y.; investigation, T.-C.T.; investigation, validation, C.-A.H.; data curation, N.-H.G.; writing—review and editing, conceptualization, supervision, and funding acquisition, S.-H.W.; conceptualization, writing—review, J.-R.Y.; visualization, H.-Y.C.; conceptualization, T.-F.C. All authors have read and agreed to the published version of the manuscript.

Funding: This research was conducted with financial support from the Ministry of Science and Technology (MOST) of Taiwan under grants MOST 110-2221-E-019-082 and MOST 111-2221-E-019-057.

Data Availability Statement: The data presented in this study are available on request from the corresponding author.

Acknowledgments: The authors would like to thank Gloria Material Technology Corp. (Taiwan) for providing the materials.

Conflicts of Interest: The authors declare that they have no known competing financial interests or personal relationships that could have appeared to influence the work reported in this paper.

References

1. Riazi, H.; Ashrafzadeh, F.; Hosseini, S.R.; Ghomashchi, R. Influence of simultaneous aging and plasma nitriding on fatigue performance of 17-4 PH stainless steel. *Mater. Sci. Eng. A* **2017**, *703*, 262–269. [[CrossRef](#)]
2. Hsiao, C.N.; Chiou, C.S.; Yang, J.R. Aging reactions in a 17-4 PH stainless steel. *Mater. Chem. Phys.* **2002**, *74*, 134–142. [[CrossRef](#)]
3. Wang, J.; Zou, H.; Li, C.; Zuo, R.; Qiu, S.; Shen, B. Relationship of microstructure transformation and hardening behavior of type 17-4 PH stainless steel. *J. Univ. Sci. Technol. Beijing Miner. Metall. Mater.* **2006**, *13*, 235–239. [[CrossRef](#)]
4. Viswanathan, U.K.; Banerjee, S.; Krishnan, R. Effects of aging on the microstructure of 17-4 PH stainless steel. *Mater. Sci. Eng. A* **1988**, *104*, 181–189. [[CrossRef](#)]
5. Stornelli, G.; Gaggia, D.; Rallini, M.; Di Schino, A. Heat treatment effect on maraging steel manufactured by laser powder bed fusion technology: Microstructure and mechanical properties. *Acta Metall. Slovaca* **2021**, *27*, 122–126. [[CrossRef](#)]
6. Chien, W.-T.; Tsai, C.-S. The investigation on the prediction of tool wear and the determination of optimum cutting conditions in machining 17-4PH stainless steel. *J. Mater. Process. Technol.* **2003**, *140*, 340–345. [[CrossRef](#)]
7. Yao, J.; Wang, L.; Zhang, Q.; Kong, F.; Lou, C.; Chen, Z. Surface laser alloying of 17-4PH stainless steel steam turbine blades. *Opt. Laser Technol.* **2008**, *40*, 838–843. [[CrossRef](#)]
8. Tavakoli Shoushtari, M.R.; Moayed, M.H.; Davoodi, A. Post-weld heat treatment influence on galvanic corrosion of GTAW of 17-4PH stainless steel in 3.5%NaCl. *Corros. Eng. Sci. Technol.* **2011**, *46*, 415–424. [[CrossRef](#)]
9. Wu, J.-H.; Lin, C.-K. Influence of high temperature exposure on the mechanical behavior and microstructure of 17-4 PH stainless steel. *J. Mater. Sci.* **2003**, *38*, 965–971. [[CrossRef](#)]
10. Gan, N.-H.; Sun, Y.-H.; Tsao, T.-C.; Li, C.-L.; Liu, J.-H.; Yen, H.-W.; Hsueh, C.-H.; Yang, J.-R.; Wang, S.-H.; Yeh, J.-W.; et al. Verification of the ability of Cu to dissolve in BCC δ in a δ - γ Solid Solution above 1200 °C and boosting δ nano-hardness in Cu-containing PHSS. *Scr. Mater.* **2022**, *211*, 114505. [[CrossRef](#)]
11. Yu, P.-J.; Huang, C.-Y.; Lin, Y.-T.; Su, Y.-C.; Yen, H.-W.; Hsu, C.-A.; Wang, S.-H.; Yeh, J.-W.; Hou, W.-H.; Lin, T.-R.; et al. Crystalline characteristics of a dual-phase precipitation hardening stainless steel in quenched solid solution and aging treatments. *Mater. Chem. Phys.* **2022**, *280*, 125804. [[CrossRef](#)]
12. Schroeder, R.; Hammes, G.; Binder, C.; Klein, A.N. Plasma debinding and sintering of metal injection moulded 17-4PH stainless steel. *Mater. Res.* **2011**, *14*, 564–568. [[CrossRef](#)]
13. Chi, Y.T.; Tsai, Y.T.; Huang, B.M.; Yang, J.R. Investigation of idiomorphic ferrite and allotriomorphic ferrite using electron backscatter diffraction technique. *Mater. Sci. Technol.* **2017**, *33*, 537–545. [[CrossRef](#)]

14. Yang, Y.; Zhan, D.; Lei, H.; Li, Y.; Qiu, G.; Wang, R.; Jiang, Z.; Zhang, H. Coupling Effect of Prior Austenite Grain Size and Inclusion Characteristics on Acicular Ferrite Formation in Ti-Zr Deoxidized Low Carbon Steel. *Metall. Mater. Trans. B* **2020**, *51*, 480–491. [[CrossRef](#)]
15. Kvackaj, T.; Bidulská, J.; Bidulský, R. Overview of HSS Steel Grades Development and Study of Reheating Condition Effects on Austenite Grain Size Changes. *Materials* **2021**, *14*, 1988. [[CrossRef](#)]
16. Capdevila, C.; Caballero Francisca, G.; García-Mateo, C.; de Andrés, C.G. The Role of Inclusions and Austenite Grain Size on Intragranular Nucleation of Ferrite in Medium Carbon Microalloyed Steels. *Mater. Trans.* **2004**, *45*, 2678–2685. [[CrossRef](#)]
17. Järvenpää, A.; Jaskari, M.; Kisko, A.; Karjalainen, P. Processing and Properties of Reversion-Treated Austenitic Stainless Steels. *Metals*. **2020**, *10*, 281. [[CrossRef](#)]
18. Bhambroo, R.; Roychowdhury, S.; Kain, V.; Raja, V.S. Effect of reverted austenite on mechanical properties of precipitation hardenable 17-4 stainless steel. *Mater. Sci. Eng. A* **2013**, *568*, 127–133. [[CrossRef](#)]
19. Vander Voort, G.F. Volume 9: Metallography and Microstructures. In *ASM Handbook*; National Institute of Standards and Technology: Gaithersburg, MD, USA, 2013; Volume 9, 493–512.
20. Tsai, Y.-T.; Lin, P.-C.; Chen, Y.-W.; Wang, S.-H.; Yang, J.-R. Fatigue behavior and microstructural characteristics of a duplex stainless steel weld metal under vibration-assisted welding. *Mater. Sci. Eng. A* **2018**, *721*, 319–327. [[CrossRef](#)]
21. Furuhashi, T.; Shinyoshi, T.; Miyamoto, G.; Yamaguchi, J.; Sugita, N.; Kimura, N.; Takemura, N.; Maki, T. Multiphase Crystallography in the Nucleation of Intragranular Ferrite on MnS+V(C, N) Complex Precipitate in Austenite. *ISIJ Int.* **2003**, *43*, 2028–2037. [[CrossRef](#)]
22. Deng, D.; Chen, R.; Sun, Q.; Li, X. Microstructural Study of 17-4PH Stainless Steel after Plasma-Transferred Arc Welding. *Materials* **2015**, *8*, 424–434. [[CrossRef](#)] [[PubMed](#)]
23. Banadkouki, S.S.G.; Yu, D.; Dunne, D.P. Age Hardening in a Cu-bearing High Strength Low Alloy Steel. *ISIJ Int.* **1996**, *36*, 61–67. [[CrossRef](#)]
24. Ke, X.; Zhang, M.; Zhao, K.; Su, D. Moiré Fringe Method via Scanning Transmission Electron Microscopy. *Small Methods* **2022**, *6*, 2101040. [[CrossRef](#)]
25. Yokozeki, S. Moiré fringes. *Opt. Lasers Eng.* **1982**, *3*, 15–27. [[CrossRef](#)]
26. Heo, Y.U.; Kim, Y.K.; Kim, J.S.; Kim, J.K. Phase transformation of Cu precipitates from bcc to fcc in Fe–3Si–2Cu alloy. *Acta Mater.* **2013**, *61*, 519–528. [[CrossRef](#)]
27. Othen, P.J.; Jenkins, M.L.; Smith, G.D.W. High-resolution electron microscopy studies of the structure of Cu precipitates in α -Fe. *Philos. Mag. A* **1994**, *70*, 1–24. [[CrossRef](#)]
28. Buswell, J.; English, C.; Hetherington, M.; Phythian, W.; Smith, G.; Worrall, G. An analysis of small clusters formed in thermally aged and irradiated FeCu and FeCuNi model alloys. In Proceedings of the Effects of Radiation on Materials: 14th International Symposium, Andover, MA, USA, 27–30 June 1990; Volume II.
29. Jesseman, R.J.; Murphy, G.J. Mechanical properties and precipitation-hardening response in ASTM A710 Grade A and A736 alloy steel plates. *J. Heat Treat.* **1984**, *3*, 228–236. [[CrossRef](#)]
30. Lee, T.H.; Kim, Y.O.; Kim, S.J. Crystallographic model for bcc-to-9R martensitic transformation of Cu precipitates in ferritic steel. *Philos. Mag.* **2007**, *87*, 209–224. [[CrossRef](#)]
31. Morito, S.; Adachi, Y.; Ohba, T. Morphology and Crystallography of Sub-Blocks in Ultra-Low Carbon Lath Martensite Steel. *Mater. Trans.* **2009**, *50*, 1919–1923. [[CrossRef](#)]
32. Yardley, V.A.; Payton, E.J. Austenite–martensite/bainite orientation relationship: Characterisation parameters and their application. *Mater. Sci. Technol.* **2014**, *30*, 1125–1130. [[CrossRef](#)]
33. Nakada, N.; Mizutani, K.; Tsuchiyama, T.; Takaki, S. Difference in transformation behavior between ferrite and austenite formations in medium manganese steel. *Acta Mater.* **2014**, *65*, 251–258. [[CrossRef](#)]
34. Wang, Z.; Chen, Y.; Jiang, C. Thermal relaxation behavior of residual stress in laser hardened 17-4PH steel after shot peening treatment. *Appl. Surf. Sci.* **2011**, *257*, 9830–9835. [[CrossRef](#)]
35. Tavakoli Shoushtari, M.R. Effect of ageing heat treatment on corrosion behavior of 17-4 PH stainless steel in 3.5% NaCl. *Int. J. Iron. Steel. Soc. Iran.* **2010**, *7*, 33–36.
36. Talebi, S.H.; Jahazi, M.; Melkonyan, H. Retained Austenite Decomposition and Carbide Precipitation during Isothermal Tempering of a Medium-Carbon Low-Alloy Bainitic Steel. *Materials* **2018**, *11*, 1441. [[CrossRef](#)]
37. Youle, A.; Ralph, B. A Study of the Precipitation of Copper from α -Iron in the Pre-Peak to Peak Hardness Range of Ageing. *Met. Sci. J.* **1972**, *6*, 149–152. [[CrossRef](#)]
38. Zielińska-Lipiec, A.; Ziewiec, A.; Tasak, E. Microstructure of Welded Joints of X5CrNiCuNb16-4 (17-4 PH) Martensitic Stainless Steel After Heat Treatment. *Arch. Metall. Mater.* **2014**, *59*, 965–970. [[CrossRef](#)]
39. Schnitzer, R.; Radis, R.; Nöhner, M.; Schober, M.; Hochfellner, R.; Zinner, S.; Povoden-Karadeniz, E.; Kozeschnik, E.; Leitner, H. Reverted austenite in PH 13-8 Mo maraging steels. *Mater. Chem. Phys.* **2010**, *122*, 138–145. [[CrossRef](#)]
40. Shiang, L.T.; Wayman, C.M. Maraging behavior of an Fe-19.5Ni-5Mn alloy II: Evolution of reverse-transformed austenite during overaging. *Metallography* **1988**, *21*, 425–451. [[CrossRef](#)]
41. Yu, P.-J.; Chen, S.-C.; Yen, H.-W.; Chang, H.-Y.; Yang, J.-R.; Wang, S.-H.; Chiu, P.-K.; Lin, T.-R. Large delta T thermal cycling induced stress accelerates equilibrium and transformation in super DSS. *Crystals* **2020**, *10*, 962. [[CrossRef](#)]

42. Pardal, J.M.; Tavares, S.S.M.; Cindra Fonseca, M.P.; Abreu, H.F.G.; Silva, J.J.M. Study of the austenite quantification by X-ray diffraction in the 18Ni-Co-Mo-Ti maraging 300 steel. *J. Mater. Sci.* **2006**, *41*, 2301–2307. [[CrossRef](#)]
43. Kim, S.-J.; Wayman, C.M. Precipitation behavior and microstructural changes in maraging Fe Ni Mn Ti alloys. *Mater. Sci. Eng. A* **1990**, *128*, 217–230. [[CrossRef](#)]
44. Sinha, P.P.; Sivakumar, D.; Babu, N.S.; Tharian, K.T.; Natarajan, A. Austenite reversion in 18 Ni Co-free maraging steel. *Steel Res.* **1995**, *66*, 490–494. [[CrossRef](#)]

Disclaimer/Publisher's Note: The statements, opinions and data contained in all publications are solely those of the individual author(s) and contributor(s) and not of MDPI and/or the editor(s). MDPI and/or the editor(s) disclaim responsibility for any injury to people or property resulting from any ideas, methods, instructions or products referred to in the content.